JGR Space Physics

Key Points:

- ubauroral polarization streams (SAPS) were observed in the same L shell region ($L = 3–4$) near the same time as 100s keV electron flux enhancements
- Proton flux enhancements were limited to lower energies and were only temporarily observed in the SAPS region
- Observations of deeper penetration for 100s keV electrons are consistent with drift paths predicted by a simple SAPS electric field model

Correspondence to:

S. Califf,
califf@colorado.edu

Author Contributions:

Conceptualization: S. Califf, H. Zhao
Data curation: M. Gkioulidou, J. W. Manweiler, D. G. Mitchell, S. Tian
Formal analysis: S. Califf, H. Zhao
Methodology: S. Califf, H. Zhao
Software: S. Califf, H. Zhao
Validation: M. Gkioulidou, J. W. Manweiler, S. Tian
Writing – original draft: S. Califf
Writing – review & editing: S. Califf, H. Zhao, M. Gkioulidou, S. Tian

Multi-Event Study on the Connection Between Subauroral Polarization Streams and Deep Energetic Particle Injections in the Inner Magnetosphere

S. Califf[1] , **H. Zhao[2]** , **M. Gkioulidou[3]** , **J. W. Manweiler[4]** , **D. G. Mitchell[3]** , **and S. Tian[5]**

[1]CIRES, University of Colorado Boulder, Boulder, CO, USA, [2]Department of Physics, Auburn University, Auburn, AL, USA, [3]Applied Physics Laboratory, Johns Hopkins University, Laurel, MD, USA, [4]Fundamental Technologies, LLC, Lawrence, KS, USA, [5]School of Physics and Astronomy, University of Minnesota, Minneapolis, MN, USA

Abstract Energetic electron flux enhancements for 100s keV energies are often observed at low L shells ($L < 4$) in the inner magnetosphere during geomagnetic storms. However, protons with similar energies do not penetrate as deeply as electrons. Electric fields from subauroral polarization streams (SAPS) have been proposed as a mechanism to explain the difference between the 100s keV electron and proton behavior by altering the particles' drift paths and allowing electrons to access lower L shells than protons. Although the primary signature of SAPS is a strong radial electric field, there are corresponding westward/eastward azimuthal electric fields on the eastern/western regions of the SAPS that cause inward/outward radial transport and a differential response between the oppositely drifting electrons and protons. We examine three events where SAPS were observed by the Van Allen Probes near the same time and L shell range as 100s keV electron enhancements deep within the inner magnetosphere. The observations demonstrate that 100s keV electrons were progressively transported radially inward and trapped at low L shells that were consistent with the spatial extent of the SAPS electric fields. Proton flux enhancements were limited to <100 keV energies and were only observed temporarily in the SAPS region, indicating that these particles were on open drift paths. The particle observations are consistent with the differential drift paths for electrons and protons predicted by a simple SAPS electric field model, suggesting that SAPS play an important role in 100s keV particle dynamics at low L shells in the inner magnetosphere.

Plain Language Summary During geomagnetic storms, high-energy charged particles become trapped in the Earth's magnetic field and drift around the Earth, with protons drifting westward and electrons drifting eastward. These particles originate in the magnetotail, which is the stretched portion of the magnetic field on the nightside of the Earth, and they are pushed earthward by electric fields. This study addresses the dynamics of charged particles near 3–4 Earth radii in the equatorial plane, where previous observations have demonstrated that electrons come closer to Earth than protons. We use measurements of electric fields, protons and electrons during three geomagnetic storms to show that the electrons behave differently than protons because of the interaction between the electric field and the opposite drift directions of the negatively and positively charged particles.

1. Introduction

Energetic particles in the Earth's inner magnetosphere display highly dynamic behavior during geomagnetic storms. Flux enhancements for electrons with 100s keV energies frequently occur deep within the inner magnetosphere ($L < 4$), even during small to moderate storms, while proton enhancements for similar energies are generally confined to larger L shells (Turner et al., 2017; Zhao, et al., 2016; Zhao et al., 2017). These particles could be considered to be in the upper energy range of the ring current (e.g., Berko et al., 1975; Daglis et al., 1999; Smith & Hoffman, 1973; Williams, 1980; Zhao et al., 2015) or the lower energy range of the radiation belts. The electron enhancements appear as inward motion of the inner edge of the outer radiation belt, and in some cases, the electrons penetrate through the slot region, providing a source population for the inner radiation belt (e.g., Reeves et al., 2016; Turner et al., 2017; Zhao & Li, 2013).

Two types of deep electron penetration have been identified: slow and fast (e.g., Su et al., 2016). Slow penetration usually occurs over several days and is believed to be caused by inward radial diffusion (e.g., Zhao & Li, 2013). Our focus is on fast penetration, which often occurs on timescales on the order of an hour or even less (e.g., Califf

et al., 2017; Zhao et al., 2017). Since the timescale of inward radial diffusion is expected to be much longer than the particle's drift period (~hours to 1 day at $L = \sim 2$–4 for 10s–100s of keV particles), fast penetration is not caused by radial diffusion. Chorus and magnetosonic waves can locally accelerate 100s keV electrons, but the timescales are on the order of hours to days, so local wave-particle acceleration is also unlikely to be the primary cause of fast penetration (e.g., Bortnik & Thorne, 2007; Horne et al., 2007).

Several mechanisms have been proposed to explain energetic particle deep penetration in the inner magnetosphere, including shock-induced radial transport, substorm injections, convection of plasma sheet particles, and inward transport of previously trapped particles by an enhanced convection electric field. Interplanetary shocks compressing the geomagnetic field can induce electric field pulses and energize energetic particles; however, such energization in the low L region requires very intense shocks that rarely occur (e.g., Kanekal et al., 2016; Li et al., 1993; Schiller et al., 2016). Substorms can inject energetic particles into the inner magnetosphere rapidly, but direct injections into $L < 4$ are also infrequent (e.g., Turner et al., 2015). Convection of plasma sheet particles is known to be an important source for protons with energies of keV to 10s of keV in the inner magnetosphere during periods of enhanced geomagnetic activity (e.g., Korth et al., 1999); however, due to the low energy of the plasma sheet populations, it is not an important immediate source for 100s keV protons and electrons (e.g., Gkioulidou et al., 2016; Zhao et al., 2015). Studies have indicated that 100s keV electron enhancements at low L shells can be explained by brief increases in the convection electric field (Califf et al., 2017; Su et al., 2016). However, a simple dawn-dusk convection electric field should have a similar effect on 100s keV protons, which is in conflict with the observations (Lejosne et al., 2018; Zhao et al., 2017).

It is known that the storm-time electric field in the inner magnetosphere is structured and dynamic. Statistical results based on near-equatorial double-probe measurements by the Combined Release and Radiation Effects Satellite (CRRES) and The Time History of Events and Macroscale Interactions during Substorms (THEMIS) revealed a region of strong electric fields in the dusk sector with a local peak between $L = 3$–6 during active times (Califf et al., 2014; Rowland & Wygant, 1998). Strong duskside electric fields were also observed in electric potential maps derived from Cluster data (Matsui, et al., 2004, 2008, 2013). This feature was attributed to sub-auroral polarization streams (SAPS), which arise through coupling between the magnetosphere and the ionosphere as field-aligned currents at the inner edge of the plasma sheet ions close poleward through a region of the ionosphere with low conductivity on the night side. SAPS create a broad region of strong radial magnetospheric electric fields, or fast westward ionospheric flow, spanning from ~18 to 04 magnetic local time (MLT) (Foster & Burke, 2002; Foster & Vo, 2002). Polarization jets (Galperin, 1973, 1974) and subauroral ion drifts (SAID) (Anderson et al., 2001; Smiddy et al., 1977; Spiro et al., 1979) are generated by a similar mechanism as SAPS but are more intense and spatially localized. We are interested in the effect of the localized radial potential drop that is common to both SAPS and SAID on energetic particle dynamics in the inner magnetosphere. SAPS are a prevalent feature of geomagnetic storms; a survey of 4 years of Super Dual Auroral Radar Network (SuperDARN) measurements reported SAPS occurring 87% of the time during moderate geomagnetic activity (−75 nT < min Dst < −50 nT) (Kunduri et al., 2017).

Lejosne et al. (2018) showed a correlation between the observations of SAPS and 100s keV electron enhancements in the inner magnetosphere in a statistical study using 1 year of data and found a relationship between the potential drop across the SAPS measured by the Van Allen Probes and the maximum energy of the electron enhancement inside $L = 4$. The authors explained the correlation between SAPS and energetic electron penetration to low L shells using a simple electric field model consisting of a dawn-dusk electric field and a radial SAPS electric field over a limited range of MLT. The opposite drift directions of electrons and protons cause electrons to gain energy and move radially inward from the SAPS potential drop, while the protons are transported radially outward and lose energy in response to SAPS, which is consistent with the observed deeper penetration for electrons in the inner magnetosphere. However, detailed event studies revealing the relation between SAPS and particle deep penetration, especially regarding the spatial and temporal distribution and the systematic differences between electron and protons, are still needed for a more advanced understanding of the effects of SAPS on inner magnetospheric energetic particle populations.

The purpose of this study is to explore the relative timing and spatial location of SAPS and differential responses in electron and proton fluxes in the inner magnetosphere in detail for specific geomagnetic storms. Using Van Allen Probes data, we focus on three events where SAPS were observed near the same time and L shell range as 100s keV electron enhancements deep within the inner magnetosphere ($L \sim 3$). The events were selected to cover

a range of geomagnetic activity and reveal similar progressive inward flux enhancements for 100s keV electrons with little variation in the 100s keV proton fluxes at low L shells.

The data used in this study are described in Section 2. Section 3 presents SAPS and energetic particle observations for the intense geomagnetic storm on 17 March 2013, and two moderate storms on 13 July 2015 and 7 September 2015 are examined in Sections 4 and 5. The connection between SAPS and the particle dynamics is discussed in Section 6, and Section 7 summarizes the results.

2. Data

We use energetic particle, electric field, and magnetic field data from the Van Allen Probes. The Magnetic Electron Ion Spectrometer (MagEIS) provides measurements of electrons of ∼30–4800 keV and ions between ∼50 keV and >1 MeV (Blake et al., 2013). We also use proton measurements from the Radiation Belt Storm Probes Ion Composition Experiment (RBSPICE) (Mitchell et al., 2013) for events in 2015, as the MagEIS ion channels suffered degradation during the mission. RBSPICE differentiates ion composition and measures protons between 20 keV and 1 MeV. Pitch-angle resolved energetic particle data were converted to phase space density by

$$f = \frac{j}{p^2} \qquad (1)$$

where j is the differential flux and p is the particle momentum. The adiabatic invariants μ, K, and L^* were derived from the Van Allen Probes MagEphem files under the external magnetic field T89D (Tsyganenko, 1989).

The electric field data are provided by the Electric Field and Waves (EFW) instrument (Wygant et al., 2013). The spin-plane wire booms measure two components of the DC electric field in the mGSE YZ plane, which are approximately aligned in the dawn-dusk and ecliptic normal directions, and the spin axis, or mGSE X component was inferred by assuming that there is no field-aligned electric field.

$$\boldsymbol{E} \cdot \boldsymbol{B} = 0 \qquad (2)$$

$$E_x = \frac{-E_y B_y - E_z B_z}{B_x} \qquad (3)$$

$\boldsymbol{B}$ is the magnetic field measured by the Electric and Magnetic Field Instrument and Integrated Science (EMFISIS) (Kletzing et al., 2013). Spacecraft vxB and the co-rotation electric fields have been subtracted to express the electric field measurements in the frame co-rotating with Earth.

$$\boldsymbol{E}_{corot\,frame} = \boldsymbol{E}_{meas} - \boldsymbol{v}_{sc} \times \boldsymbol{B} + (\boldsymbol{\omega}_E \times \boldsymbol{r}) \times \boldsymbol{B} \qquad (4)$$

$\boldsymbol{\omega}_E$ is the angular velocity of the Earth, $\boldsymbol{v}_{sc}$ is the spacecraft velocity, and $\boldsymbol{r}$ is the spacecraft position. The radial and azimuthal electric field components are defined in a coordinate system relative to the local magnetic field.

$$\hat{e}_b = -\frac{\boldsymbol{B}}{|\boldsymbol{B}|} \qquad (5)$$

$$\hat{e}_{az} = \frac{\hat{e}_b \times \boldsymbol{r}}{|\hat{e}_b \times \boldsymbol{r}|} \qquad (6)$$

$$\hat{e}_r = \hat{e}_{az} \times \hat{e}_b \qquad (7)$$

The radial direction points away from the Earth perpendicular to the local magnetic field. The azimuthal direction is westward, so a positive azimuthal electric field causes a radially inward ExB drift.

Spin-averaged particle measurements from the Helium, Oxygen, Proton, and Electron Mass Spectrometer (HOPE) (Funsten et al., 2013) are also used to identify the location of the inner edge of the 10s keV proton and electron boundaries, which are important for the generation of SAPS. Plasma density derived from the upper hybrid line is provided in the EMFISIS L4 data (Kurth et al., 2015) and is used to identify the plasmapause.
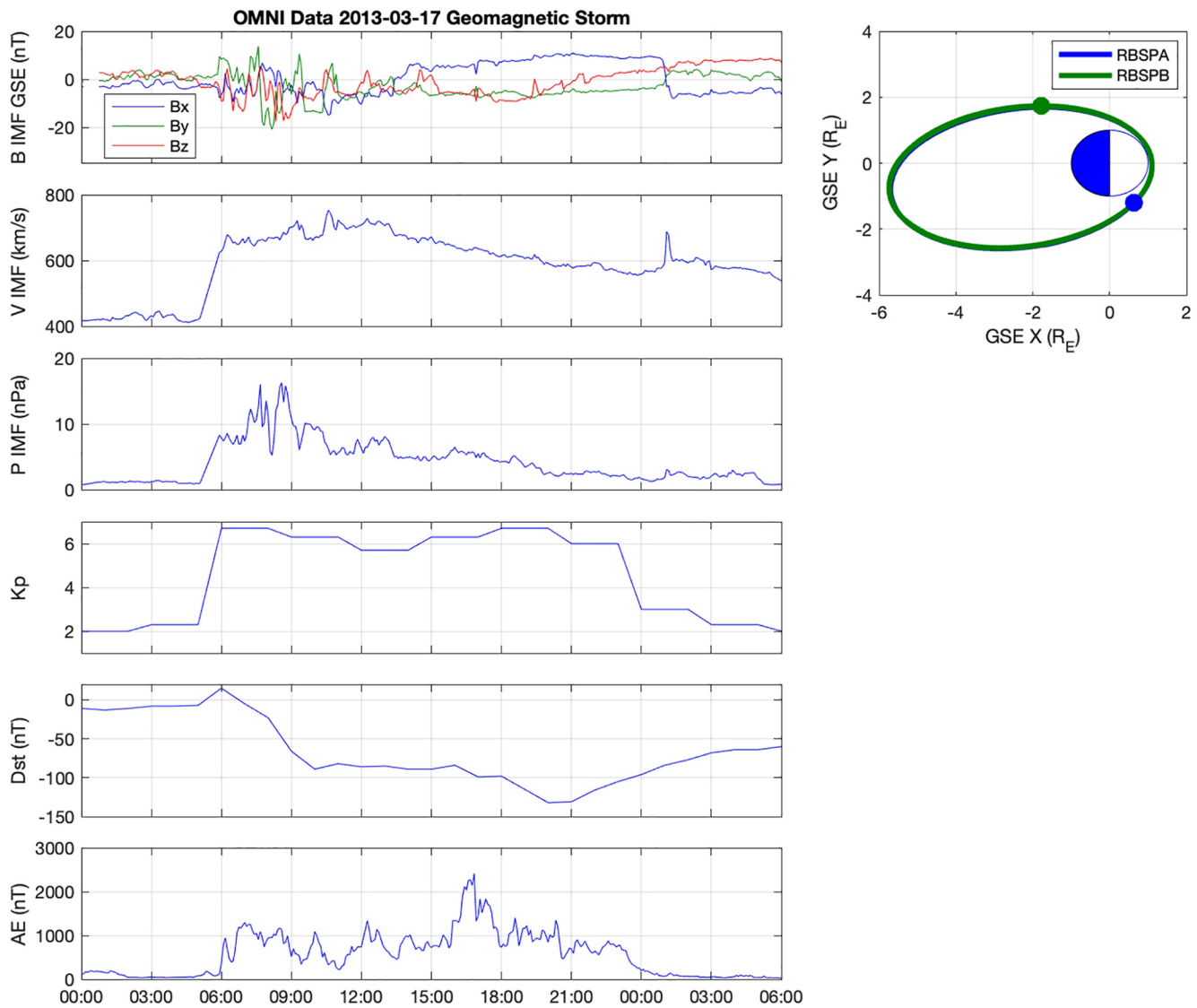
Figure 1. Solar wind measurements, geomagnetic indices, and Van Allen Probes orbits during the 17 March 2013 geomagnetic storm.

3. Event 1: 17 March 2013

Figure 1 shows an overview of the solar wind conditions, geomagnetic indices, and the Van Allen Probe orbits during the 17 March 2013 geomagnetic storm. A coronal mass ejection (CME) impacted the Earth's magnetosphere at 06 UT, initiating an intense geomagnetic storm with minimum Dst = −132 nT that has been studied extensively (e.g., Foster et al., 2014; Lyons et al., 2016; Yu et al., 2015). We focus on SAPS/SAID and energetic particle flux enhancements at low L shells during the main phase of the storm between 06 and 20 UT. The Van Allen Probes sampled $L = 3$ near 21 MLT on outbound passes and 04 MLT on inbound passes, and RBSPA trailed RBSPB by approximately 1.5 hr.

An overview of the energetic electron and ion fluxes measured by the Van Allen Probes are plotted in Figure 2 for the 17 March 2013 geomagnetic storm. MagEIS does not differentiate ion composition, but the measurements cover a more complete range of L shells than the RBSPICE proton fluxes during this event due to missing RBSPICE data. Therefore, we present the MagEIS ion data with the interpretation that it qualitatively reflects spatial variations in the proton fluxes. Prior to the beginning of the storm at 06 UT, the 100s keV electrons displayed a typical radiation belt structure consisting of an inner and outer belt separated by the slot region where fluxes are low. As the storm progressed, the inner edge of the outer belt moved radially inward rapidly (black dashed line,
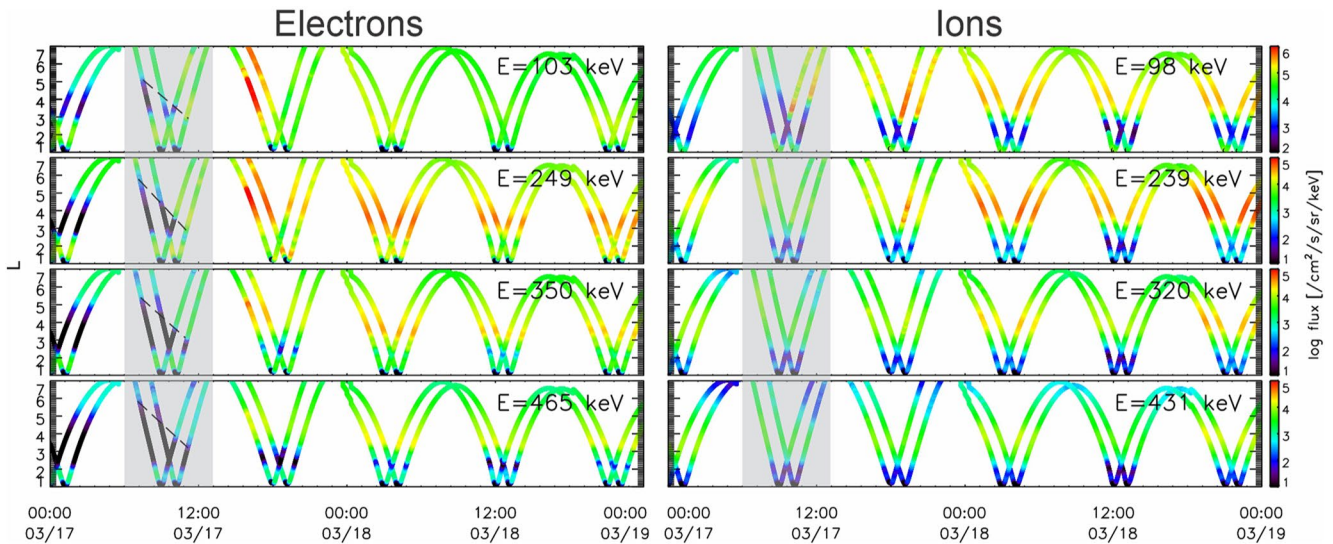
Figure 2. Spin-averaged electron (left) and ion (right) fluxes during the 17 March 2013 geomagnetic storm. The shaded regions indicate orbits where the electrons initially penetrated to low L shells and SAPS were observed on outbound post-dusk passes.

Figure 2), resulting in large flux enhancements at lower L shells within a few hours, filling the slot region for energies between 100 and 465 keV. The ion enhancements occurred at lower energies and did not penetrate as deeply as the electrons. These differences are more apparent in the radial flux and phase space density plots shown in Figures 3 and 4. We focus on consecutive outbound duskside (21 MLT) passes between ∼0900 and 1400 UT on 3/17 where SAPS were observed by both RBSP spacecraft concurrently with large electron flux enhancements at low L shells. Note that we are not able to observe SAPS features on dawnside inbound passes during this event, as SAPS are preferentially located in the post-dusk sector (e.g., Foster & Vo, 2002).

Figure 3 displays the electron and ion fluxes sorted by L shell for the passes surrounding the low-L flux enhancements from ∼04 UT to 18 UT on March 17. Inbound predawn measurements are plotted without markers, and outbound post-dusk measurements are plotted with circles. Electron fluxes progressively increased at lower L shells between passes, and the lower energy electrons penetrated to lower L shells. For 103 keV electrons, the inner boundary of flux enhancements was near $L = 2.4$, while 465 keV electron enhancements reached $L = 2.7$ during this period. The blue and green lines correspond to the outbound passes with SAPS observations of interest. Electron fluxes for energies between 103 and 465 keV increased by orders of magnitude near $L = 3$–4 between these two passes, which were only ∼1.5 hr apart.

The ion fluxes show a dramatically different response, with little variation below $L = 4$ in the fluxes above 98 keV. On the RBSPB post-dusk outbound pass prior to the electron flux enhancement (blue line), elevated fluxes for 98 keV ions were observed inside $L = 3$, but on the next pass through the same local time by RBSPA, the inner 98 keV flux boundary retreated to $L > 3.5$. This is in contrast to the persistent inward motion of the electron flux boundary and sustained electron flux at low L shells. The elevated ion fluxes on the last pass in Figure 3 (red line) are likely caused by the spacecraft sampling different magnetic latitudes on each orbit, rather than reflecting real changes in the 100s keV ion population at low L shells. This interpretation is supported by the radial phase space density profiles introduced in Figure 4.

To further investigate the evolution of the energetic particle populations in the inner magnetosphere, we converted flux measurements to phase space density according to Equation 1. We assume that the ion fluxes are dominated by protons for the phase space density calculation and note that we are interested in the relative change in phase space density between orbits. Figure 4 shows the radial phase space density profiles for electrons and ions for constant values of μ and K in a similar format to the flux measurements in Figure 3. The electrons had a steep outward radial gradient in phase space density that shifted to lower L shells during the storm, with deeper inward penetration occurring for lower values of μ. These observations are consistent with inward radial transport, as the general phase space density gradient for constant first and second adiabatic invariants is preserved and moves progressively to lower L shells. On the first outbound pass (blue lines), the inner edges of the steep electron phase
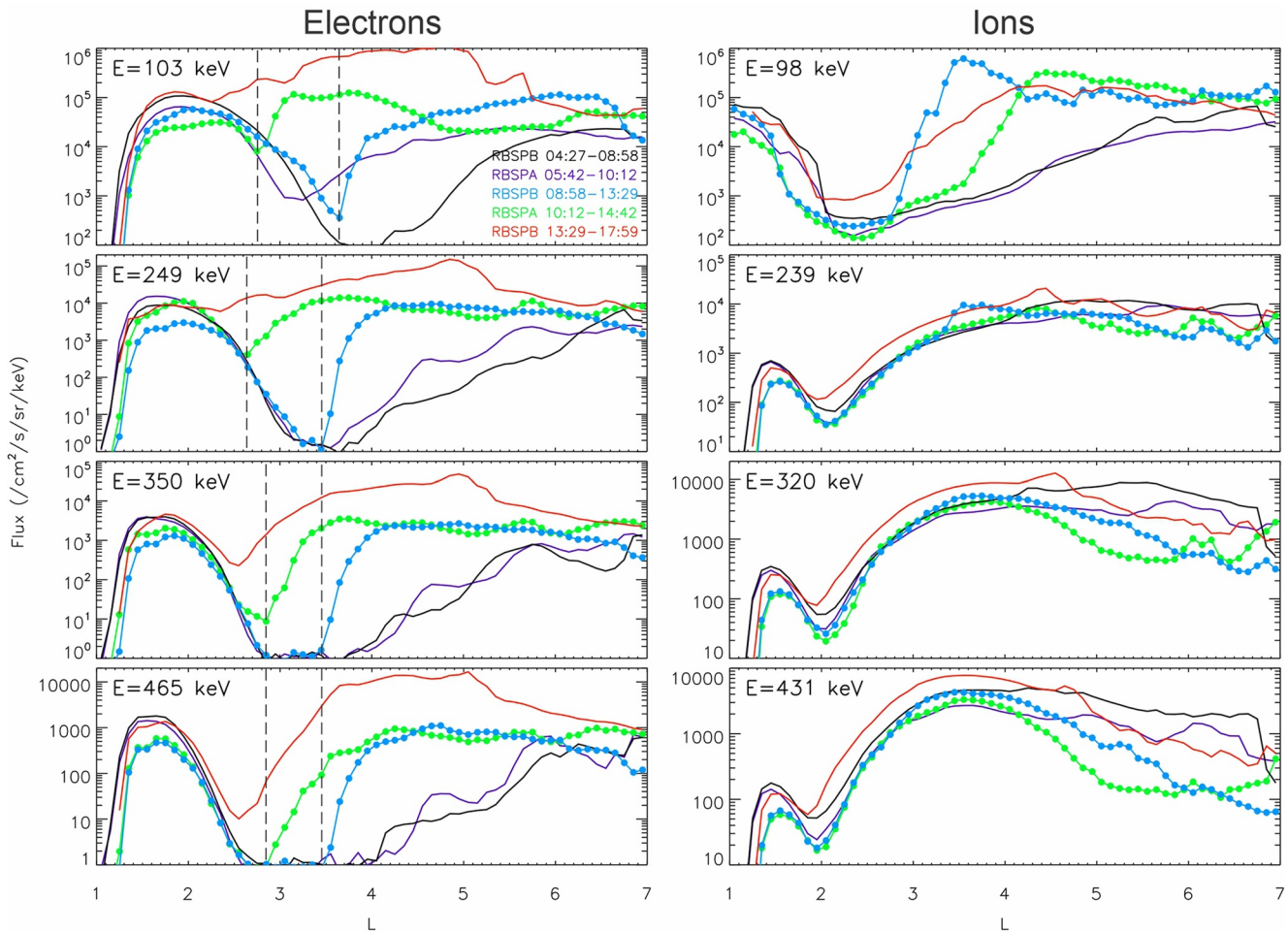
Figure 3. Spin-averaged electron (left) and ion (right) fluxes sorted by L shell for Van Allen Probes orbits on 17 March 2013. Outbound duskside (21 MLT at $L = 3$) passes are plotted with closed circles, and inbound dawnside (04 MLT at $L = 3$) passes are plotted without markers.

space density gradient for $\mu = 10$–50 MeV/G were all located near $L = 3.1$. On the next outbound pass 1.5 hr later, the inner edge of the steep gradients moved to $L = 2.5$ for 10 MeV/G electrons and $L = 2.7$ for 50 MeV/G electrons. On the following inbound dawnside pass (red line, Figure 4), the inner edge of the electron phase space density gradient moved further inward, indicating that the electrons were trapped at low L shells.

For ions, the phase space density radial gradient was more gradual, and there was much less variation during this period. On the first outbound pass, there was an enhancement in the 10 MeV/G ion phase space density at $L > 2.9$ that was earthward of the inner 10 MeV/G electron boundary. However, the inner ion phase space density boundary retreated to $L = 3.4$ on the next outbound pass, in contrast to the 0.4–0.6 L inward displacement for electrons at the same time.

The flux and phase space density profiles reveal that electrons were able to reach lower L shells than ions with similar energies during this event. Also, the electron flux enhancements were sustained and moved progressively inward, while the ~100 keV ions showed brief enhancements at lower energies that did not persist on subsequent passes. The electron observations alone could suggest that the low-L flux enhancements can be caused by large-scale inward radial transport due to variations in the convection electric field. However, if the electron enhancements were caused by a simple increase in a symmetric dawn-dusk convection electric field, we would expect a similar response in the ions, which was not observed.

Figure 5 shows the electric field measured by the Van Allen Probes during the two outbound post-dusk passes where the electron flux increased significantly at low L shells. At 9:52 UT, a strong radial electric field was observed near the plasmapause by RBSPB spanning $L = $ ~2.3–3.3 (left panels), with a peak amplitude of 40 mV/m
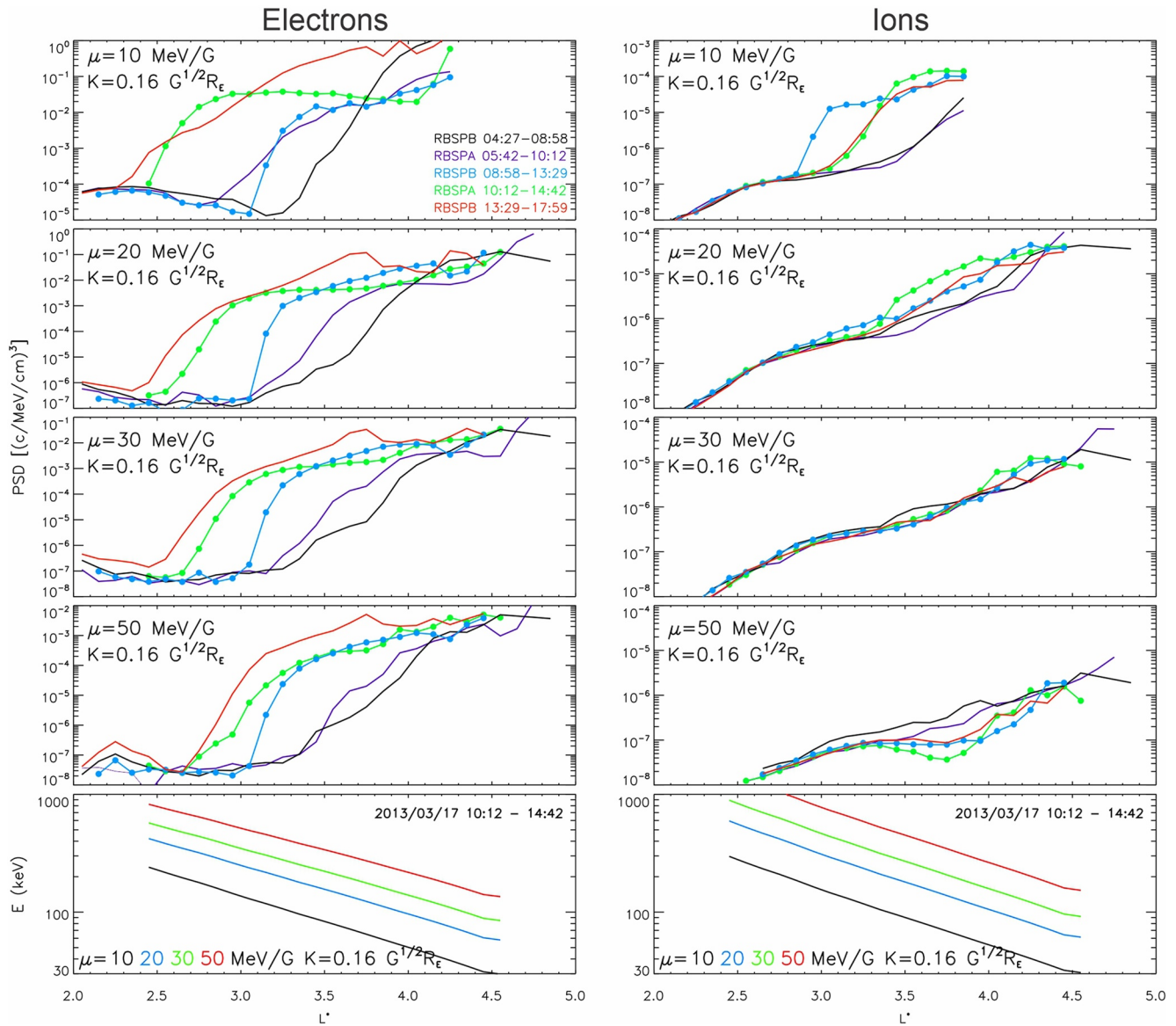
Figure 4. Phase space density as a function of L shell for electrons (left) and ions (right) on 17 March 2013. The bottom panels show the relationship between the first adiabatic invariant, μ, and particle energy. Outbound duskside passes (21 MLT at $L = 3$) are plotted with closed circles, and inbound dawnside (04 MLT at $L = 3$) passes are plotted without markers.

at $L = 3$. The plasmapause at $L = {\sim}3.2$ is identified by the steep radial density gradient, where the density decreased rapidly from >1,000 cc to <100 cc within 0.02 L ($\sim$100 km). We define the SAPS region to begin at the inner edge of the 10s keV ions at $L = 2.7$ (panel d), and it encompasses the broad radial electric field enhancement extending to $L = 3.2$ (panel a) with an amplitude of $\sim$10 mV/m. The more intense electric field at $L = 3.1$ is a SAID, which we interpret as a transient feature occurring within the more persistent and broad SAPS region. There is an ion enhancement up to 200 keV associated with the SAID, and a narrow separation between the ion and electron boundaries (panels c and d). The electric field also penetrated to lower L shells, inside of the 10s keV ion boundary, with an amplitude of 2 mV/m at $L = 2.3$. The SAPS/SAID electric field was mostly radial, but there was a negative azimuthal (eastward) component as well. This negative azimuthal electric field creates a radially outward ExB drift in the dusk sector that transports the ions in the SAPS region to larger L shells as they drift westward.
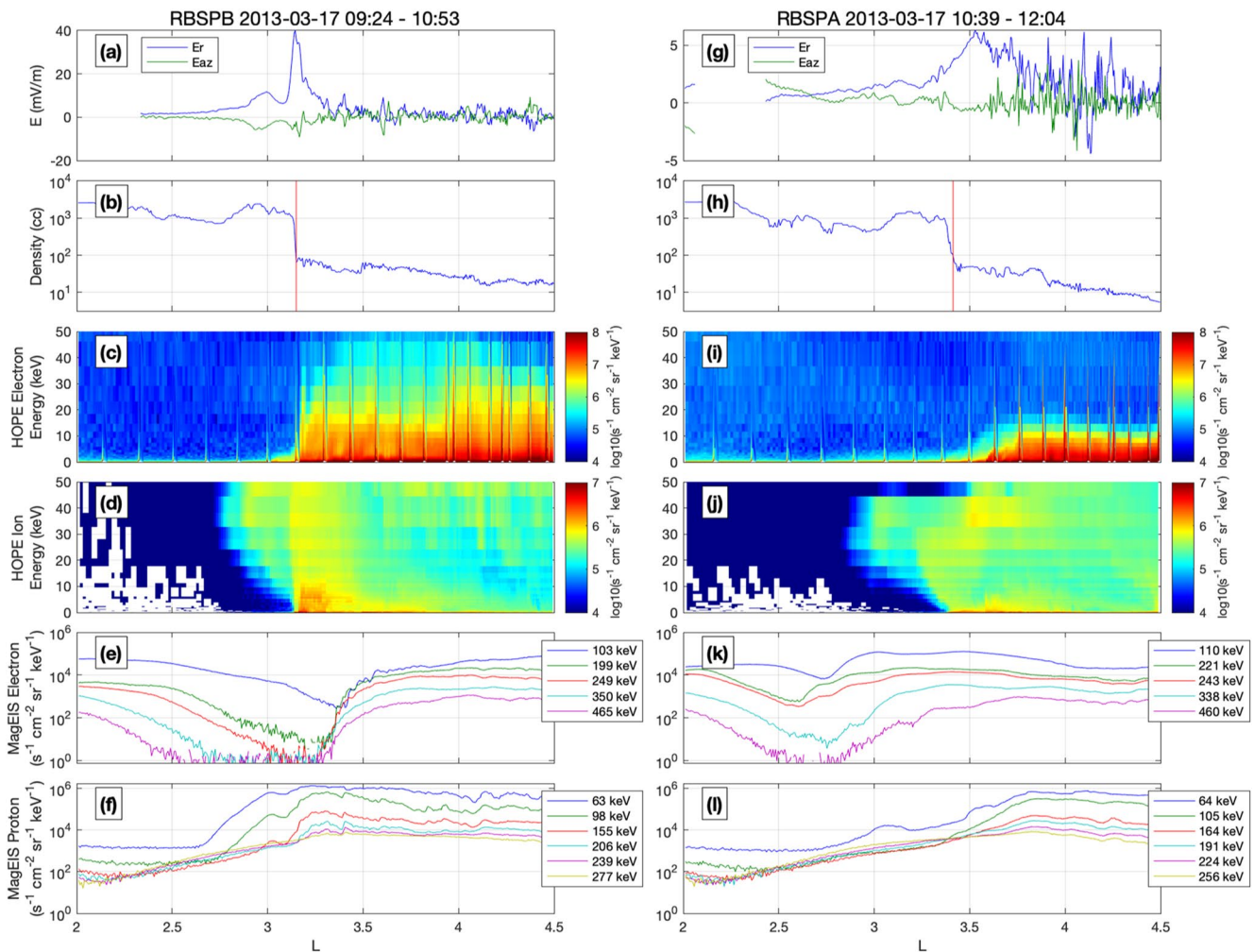
Figure 5. SAPS measurements from consecutive duskside (21 MLT at $L = 3$) passes by RBSPB (left panels) and RBSPA (right panels) on 17 March 2013. (a, g) Radial and azimuthal components of the electric field in the frame co-rotating with Earth, (b, h) plasma density with the plasmapause marked by a red line, (c, i) <50 keV electron fluxes, (d, j) <50 keV proton fluxes, (e, k) 100s keV electron fluxes, and (f, l) 100s keV proton fluxes.

Approximately 1.5 hr later, RBSPA observed an enhanced radial electric field spanning from $L = 3$–3.7 with a peak amplitude of 7 mV/m at $L = 3.5$ on an outbound pass through the same local time as RBSPB. The relative boundaries of the SAPS electric field and keV particles are similar to the previous RBSPB pass, as the inner edge of the electric field enhancement is correlated with the inner edge of the keV ions, and the keV electron boundary is located just outside of the peak electric field. These consecutive passes reveal a broad region of strong SAPS electric fields at low L shells that persists for at least 1.5 hr and also highlight significant variability in the intensity and spatial structure of the SAPS.

During the first RBSPB pass, the inner edge of outer electron radiation belt for energies of 103–465 keV was observed at $L = 3.4$ (panel e), near the outer edge of the SAPS electric field. On the next pass, these boundaries moved inward to $L = 2.7$–2.8 (panel k), which is close to the inner edge of the strong SAPS/SAID electric field observed on the first pass. The protons showed an opposite response, where the flux boundaries moved radially outward between the first and second passes. There were elevated fluxes near $L = 2.7$–2.8 for 63–98 keV protons on the first pass that were correlated with the inner SAPS electric field peak and flux enhancements up to 206 keV coincident with the strong SAID electric field at $L = 3.2$ (which can also be seen in Figure 3). On the next pass, all of the proton fluxes were significantly reduced inside $L = 3.5$, which suggests that protons associated with the SAPS were on open drift paths.

Around the same time that RBSPB was crossing the SAPS region on the duskside, RBSPA was on an inbound pass through the dawnside inner magnetosphere. Although not shown here, we note that at 09:35 UT RBSPA crossed the plasmapause near dawn at $L = 2.7$ and observed 1–2 mV/m dawn-dusk electric fields, 27 min before RBSPB passed through the strong SAID electric field on the dusk side. THEMIS A also observed the plasmapause at $L = 2.8$ at 10:00 UT near 03 MLT, and there were 2–4 mV/m dawn-dusk electric field enhancements at low L shells outside the plasmasphere. These supporting observations demonstrate that there were strong and variable convection electric fields at low L shells shortly before 100s keV electron fluxes increased in the same region. The dawnside plasmapause, inner boundary of the duskside plasma sheet ions, and the inner boundary of the SAPS electric field were all observed at $L = 2.7$, which aligns with the inner L extent of the 100s keV electron enhancements.

If the electric field were simply described by a dawn-to-dusk electric field that penetrated to low L shells during this event, we would expect both electrons and ions to be transported radially inward on the nightside. In this scenario, electrons and ion enhancements would have been observed at similar L shells, and both species would have been trapped due to the symmetry of the electric field and the resulting particle drift paths. However, we observed strong radial SAPS electric fields in the post-dusk sector, which clearly differ from a uniform dawn-to-dusk convection electric field. The SAPS electric field causes westward drifting ions to be transported radially outward in the post-dusk sector, while eastward drifting electrons are transported radially inward and are trapped at low L shells in the predawn sector. The effect of SAPS on the particle drift paths will be discussed in more detail in Section 6.

4. Event 2: 13 July 2015

Next, we examine energetic particle enhancements and SAPS electric fields during the main phase of a moderate storm (minimum Dst = −59 nT) on 13 July 2015. Although this event is much weaker than the 17 March 2013 storm, there are striking similarities in the electron and proton flux progression in the inner magnetosphere and their relationship to SAPS electric fields. During this event, the Van Allen Probes sampled the dusk side SAPS region on inbound passes near 21 MLT, and the outbound passes provided observations at low L shells near 14 MLT.

The time evolution of radial profiles of phase space density during this event are shown in Figure 6. For this event, we derived the proton phase space density from RBSPICE proton flux measurements. The circles represent measurements from outbound dayside passes, and the inbound duskside data are plotted without markers. The electron phase space density had an outward radial gradient that consistently moved inward during the interval when SAPS were present. The initial phase space density enhancement at $L > 3.1$ for 10 MeV/G electrons was observed by RBSPB on an outbound dayside pass (green line), approximately 2 hr after the spacecraft had encountered SAPS on the inbound duskside portion of the orbit. On the same pass, the phase space density increased for 20–50 MeV electrons between $L = 4$–5, but not at lower L shells. Three hours later, these steep higher-energy electron phase space density gradients had moved inward to $L = 3$-3.4 (yellow lines), corresponding to flux enhancements up to 354 keV in the slot region. In contrast, 20–50 MeV/G proton phase space density showed little variation during this period. The 10 MeV/G protons reveal a local time dependence, with larger phase space density consistently measured on the inbound duskside passes than on the outbound dayside passes.

Figure 7 shows SAPS electric fields measured by both spacecraft on inbound passes near 21 MLT separated by approximately 4 hr. The first RBSPB pass corresponds to the black lines in Figure 7, which occurred prior to the energetic electron enhancements at low L shells and near the beginning of the main phase of the storm. The following SAPS observation by RBSPA corresponds to the yellow lines in Figure 6 where enhanced energetic electron fluxes were measured down to $L = 3$. We could not reliably extract the radial electric field for inbound passes later in the day because the spacecraft spin plane was too close to the magnetic field vector, but all of the inbound duskside passes showed elevated dawn-dusk electric fields near the plasmapause, suggesting that SAPS were present throughout the day as the 100s keV electrons continued to progress to lower L shells.

During the first RBSPB SAPS observation, the plasmapause was located at $L = 4.2$, and the SAPS electric field spanned from the inner 20 keV ion boundary at $L = 3.2$ to the outer edge of the enhanced radial electric field at $L = 4.6$. On the following RBSPA pass, the plasmapause moved to $L = 4.1$, and the inner 20 keV ion boundary was located below $L = 3$. The peak radial electric field was 5–6 mV/m in both cases. The inner boundary of
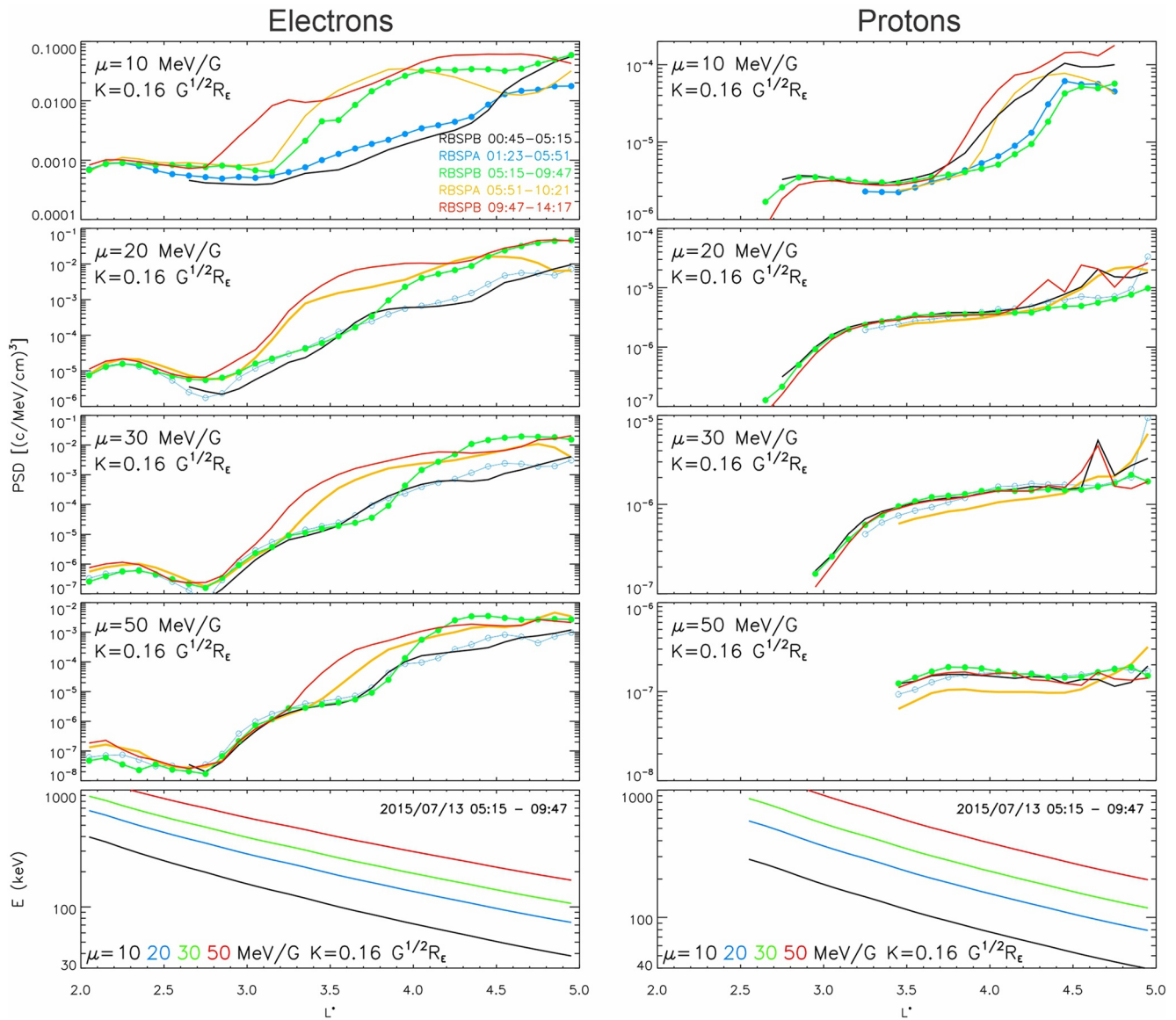
Figure 6. Phase space density as a function of L shell for electrons (left) and protons (right) on 13 July 2015. Outbound dayside passes (14 MLT at $L = 3$) are plotted with circles, and inbound duskside (21 MLT at $L = 3$) passes are plotted without markers. The bottom panels show the relationship between the first adiabatic invariant, μ, and particle energy.

SAPS electric field was closely correlated with the inner boundary of the energetic electron enhancements during this period, again suggesting a critical role of the SAPS electric field in electron deep penetration, and proton responses during this event were also lacking. Similar to the previous event, the radial electric field enhancement penetrated inside of the inner edge of the plasma sheet ions, and both spacecraft also observed negative azimuthal electric fields in the post-dusk SAPS region. The negative azimuthal electric field transports particles radially outward in the dusk sector, and is a critical component to the differential response of the electrons and protons. In Section 6, we show that potential patterns derived from a SAPS electric field model predict corresponding westward electric fields on the dawnside that transport eastward drifting electrons radially inward.
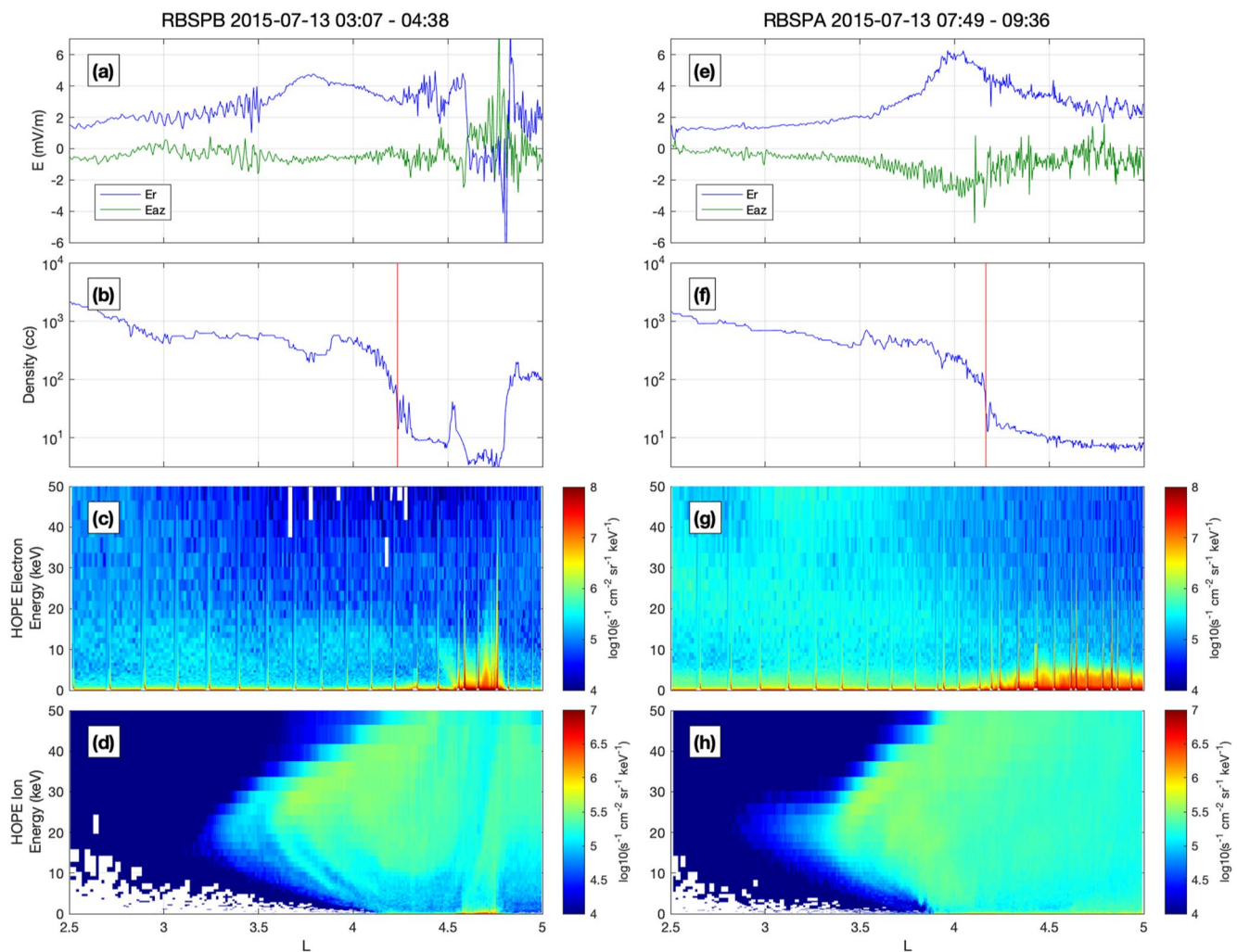
Figure 7. SAPS measurements from consecutive duskside (21 MLT at $L = 3$) passes by RBSPB (left panels) and RBSPA (right panels) on 13 July 2015. (a), (e) Radial and azimuthal components of the electric field in the frame co-rotating with Earth, (b), (f) plasma density with the plasmapause marked by a red line, (c), (g) <50 keV electron fluxes, and (d), (h) <50 keV proton fluxes.

5. Event 3: 7 September 2015

The third event that we investigate occurred during a moderate geomagnetic storm on 7 September 2015 with minimum Dst $= -70$ nT. The Van Allen Probes orbits were in a similar local time to the 13 July 2015 event, with inbound passes sampling the post-dusk sector at $L = 3$ near 20 MLT and the outbound passes sampling the dayside near 12 MLT. Figure 8 shows the radial phase space density profiles for electrons and protons, where the proton phase space density was computed from RBSPICE proton fluxes. The overall picture is similar to the first two events – the electron fluxes progressively increased at lower L shells, with the inner boundary of the gradient reaching $L = 2.5$ for 10 MeV/G electrons and $L = 2.8$ for 50 MeV/G electrons, corresponding to enhanced electron fluxes up to 470 keV in the slot region. The proton phase space density gradient was not as steep as the electron gradient, and the phase space density remained stable below $L = 4$ with brief enhancements on the dusk side at lower energies.

On the inbound passes where SAPS were observed (blue and green lines), the 10–30 MeV/G proton phase space density increased between $L = 3.2$–4, but the elevated phase space density was not present at low L shells on following dayside passes, suggesting that these protons were on open drift paths. Consistent with the previous examples, the electron phase space density profiles demonstrate that the electrons are transported radially inward
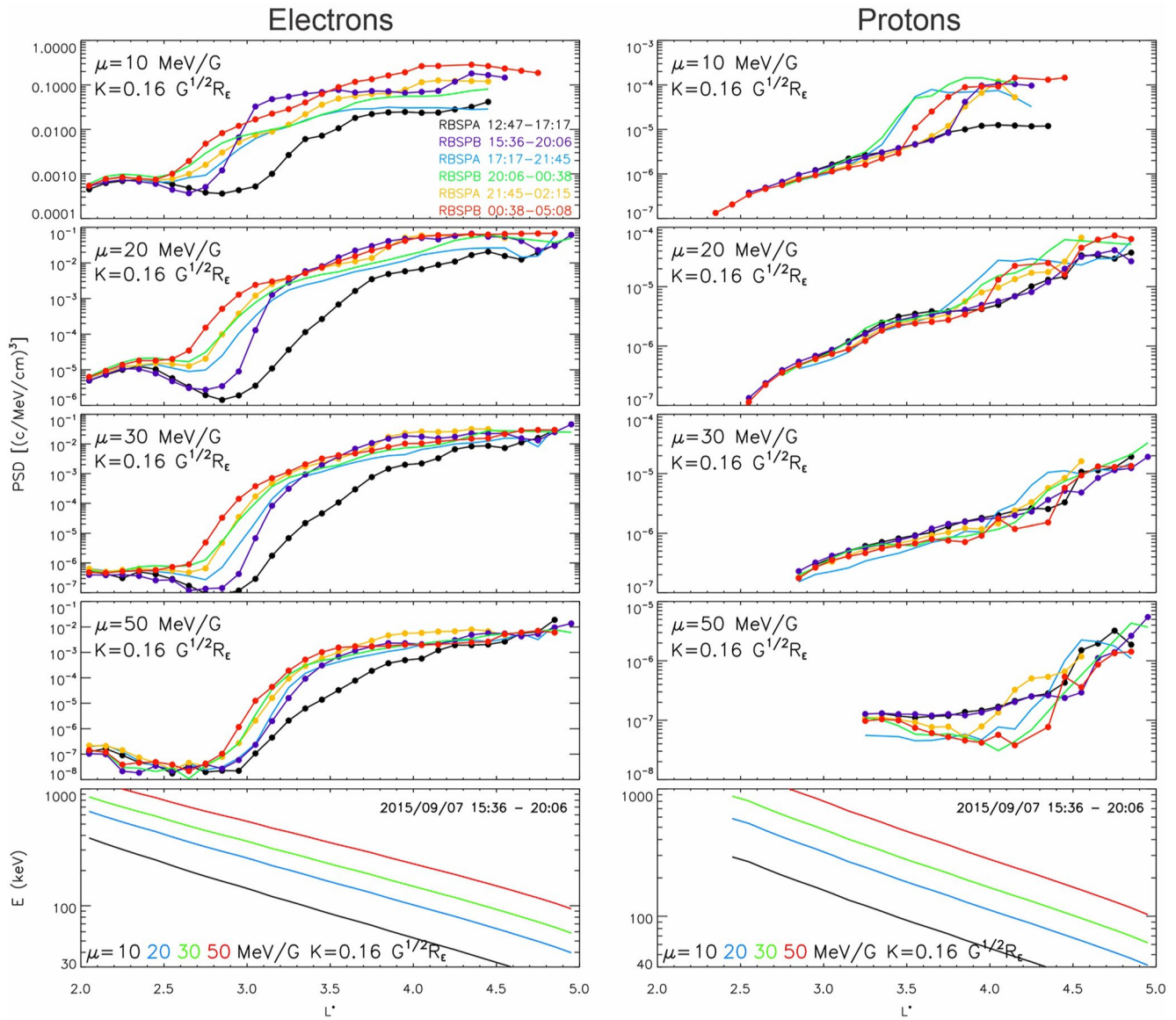
Figure 8. Phase space density as a function of L shell for electrons (left) and protons (right) on 7 September 2015. Outbound dayside (12 MLT at $L = 3$) passes are plotted with circles, and inbound duskside (20 MLT at $L = 3$) passes are plotted without markers. The bottom panels show the relationship between the first adiabatic invariant, μ, and particle energy.

and trapped at low L shells, while the proton phase space density profiles show little variation in the same region of the inner magnetosphere during intervals when SAPS are present.

SAPS electric field observations are displayed in Figure 9 for consecutive post-dusk inbound passes by both RBSP spacecraft. These passes correspond to the blue and green lines in Figure 8, approximately 2 hr after the initial low-L energetic electron flux enhancement was observed on the dayside by RBSPB at 16:30 UT. Clear SAPS features were not present on the inbound passes preceding these observations, suggesting the formation of SAPS somewhere in between. Although the timing of the orbits did not allow the SAPS region to be sampled prior to the initial flux enhancement, the electrons continued to move radially inward during and after the time that the SAPS observations were available.

First, RBSPA observed a broad radial electric field enhancement between $L = 3$–3.9, with a peak electric field of 7 mV/m outside of the plasmapause near $L = 3.7$. The 30 keV protons reached $L = 2.5$, and a more intense 10s keV proton flux enhancement was correlated with the gradual increase in the electric field at $L = 3$. On the
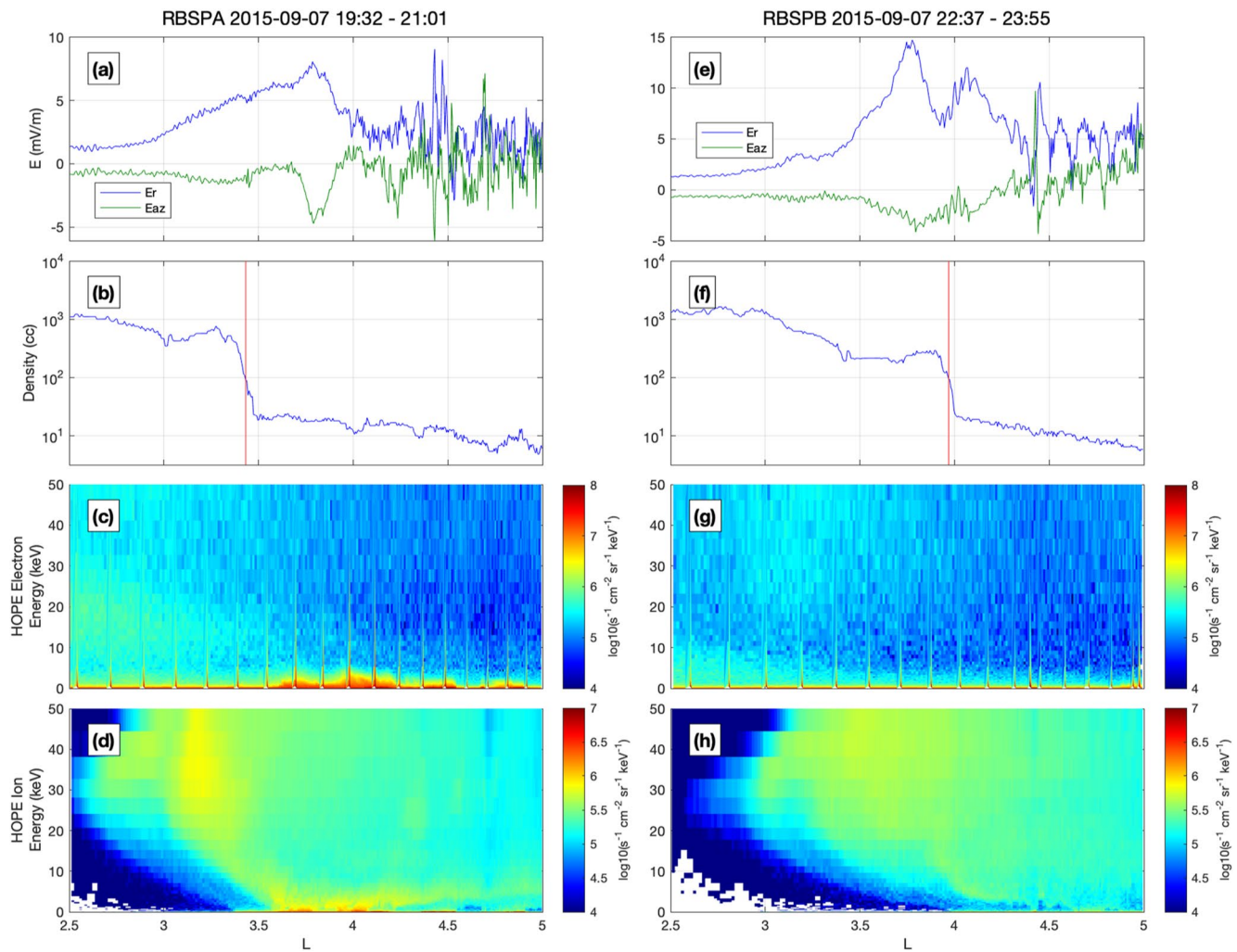
Figure 9. SAPS measurements from consecutive duskside (20 MLT at $L = 3$) passes by RBSPB (left panels) and RBSPA (right panels) on 7 September 2015. (a, e) Radial and azimuthal components of the electric field in the frame co-rotating with Earth, (b, f) plasma density with the plasmapause marked by a red line, (c, g) <50 keV electron fluxes, and (d, h) <50 keV proton fluxes.

following RBSPB inbound pass, the SAPS electric field spanned a similar spatial region with a peak amplitude of 14 mV/m. Both spacecraft also observed a lower-amplitude radial electric field penetrating to at least $L = 2.5$, and a negative azimuthal component, consistent with the previous examples. The inner plasma sheet ion boundaries and electric field enhancements are spatially consistent with the inward penetration of the steep electron phase space density gradients.

6. Discussion

The three events examined in this study show a correlation between energetic electron flux enhancements at low L shells and SAPS electric fields. In each event, the 100s keV electron fluxes progressively increased at lower L shells, with lower energies reaching the lowest L shells, and the inner boundary of the electron enhancements was consistent with the location of the SAPS electric field. Radial phase space density profiles for electrons revealed a steep radial gradient that moved earthward between observations, suggesting that the flux enhancements were caused by inward radial transport. 100s keV proton fluxes, on the other hand, had almost no variation in the low-L region. Lower-energy (<100 keV) proton flux enhancements did occur on the dusk side coincident with SAPS during some events, but the fluxes did not remain elevated on following passes.

The convection electric field is generally described by a large-scale dawn-dusk electric field that is driven by magnetospheric reconnection with the solar wind. This creates sunward flow that brings plasma sheet particles from the magnetotail into the inner magnetosphere, providing the source population for the ring current and radiation belts. For 100s keV particles, periodic enhancements in convection can alter the drift paths and allow particles to be trapped at progressively lower L shells. However, the symmetric dawn-dusk convection electric field should have a similar effect on 100s keV protons and electrons, which is in conflict with the observations.

Lejosne et al. (2018) showed that SAPS can allow energetic electrons to access lower L shells than protons with similar energies using a simple model of the SAPS electric potential combined with the Volland-Stern electric field model (Stern, 1975; Volland, 1973). The Volland-Stern potential is given by

$$V_{VS} = -\frac{a}{r} - br^\gamma \sin\phi \tag{8}$$

where $a = -89.4\ kV$ is the corotation potential, r is the radial distance in the equatorial plane, γ is the shielding factor, and we use $\gamma = 2$ as suggested by some previous studies (e.g., Maynard & Chen, 1975), ϕ is the angle east of midnight, and b is a K_p-dependent term given by (Maynard & Chen, 1975)

$$b = \frac{0.045}{(1 - 0.159K_p + 0.0093K_p^2)^3}\ \left(\frac{kV}{R_E^2}\right) \tag{9}$$

The SAPS model describes a radial potential drop that is confined to a limited range of L and MLT.

$$V_{\text{SAPS}}(L,\phi) = V_{\text{peak}} f(L) g(\phi) \tag{10}$$

$$f(L) = \frac{1}{2}\left(1 + \sin\left(\frac{\pi}{2}\left\{\frac{L - L_0}{\Delta L}\right\}\right)\right) \tag{11}$$

$$g(\phi) = \cos^2\left(\frac{\pi}{2}\left\{\frac{\phi - \phi_0}{\Delta\phi}\right\}\right) \tag{12}$$

This is a simplified version of the SAPS model developed by Goldstein et al. (2005) that was shown to reproduce dynamics of the plasmasphere. We compute the particles' 2D drift paths in the equatorial plane using the electric field models and a dipole representation of the equatorial magnetic field strength, B_0.

$$B_0 = B_E\left(\frac{R_E}{r_0}\right)^3 \tag{13}$$

B_E is the equatorial magnetic field strength at the surface of the Earth, and R_E is the Earth's radius.

Figure 10 compares the drift paths for 10 MeV/G electrons and protons at the magnetic equator under the influence of the Volland-Stern electric field model (left panels), and the combined Volland-Stern and SAPS electric field (right panels). The Volland-Stern parameters are $K_p = 6$ and $\gamma = 2$, and the SAPS model assumes a 40 kV potential drop between $L = 2.8$–3.4 centered at 21 MLT with a width of 8 MLT. These parameters were chosen to be representative of the storm-time convection electric field and SAPS during 17 March 2013 event to qualitatively illustrate the impact of SAPS on the drift trajectories. The separatrices of open and closed drift paths are shown in red dashed lines, and the two dotted circles show $L = 4$ and $L = 6$, respectively.

In the case of the Volland-Stern electric field model (Figure 10, left panels), the electrons reach the lowest L shells at dawn, and the protons reach the lowest L shells at dusk. Open drift paths for electrons originating in the postdusk-midnight sector reached $L \sim 4$ in the inner magnetosphere. These electrons drift eastward around the dayside, remaining at low L shells, and then exit the inner magnetosphere in the afternoon sector. The corresponding open proton drift paths enter in the midnight-predawn sector, drift westward and reach slightly lower L shells ($L \sim 3.5$) than the electrons before exiting between noon and dawn. Assuming a uniform source population in the plasma sheet, this convection electric field would result in similar flux enhancements for electrons and protons at low L shells during periods of increased convection, with proton enhancements occurring earthward of the electron enhancements.

When the SAPS electric field is included (Figure 10, right panels), the drift paths become skewed. The open drift paths for electrons reach lower L shells ($L \sim 3.5$) with SAPS than for the Volland-Stern model alone, and they
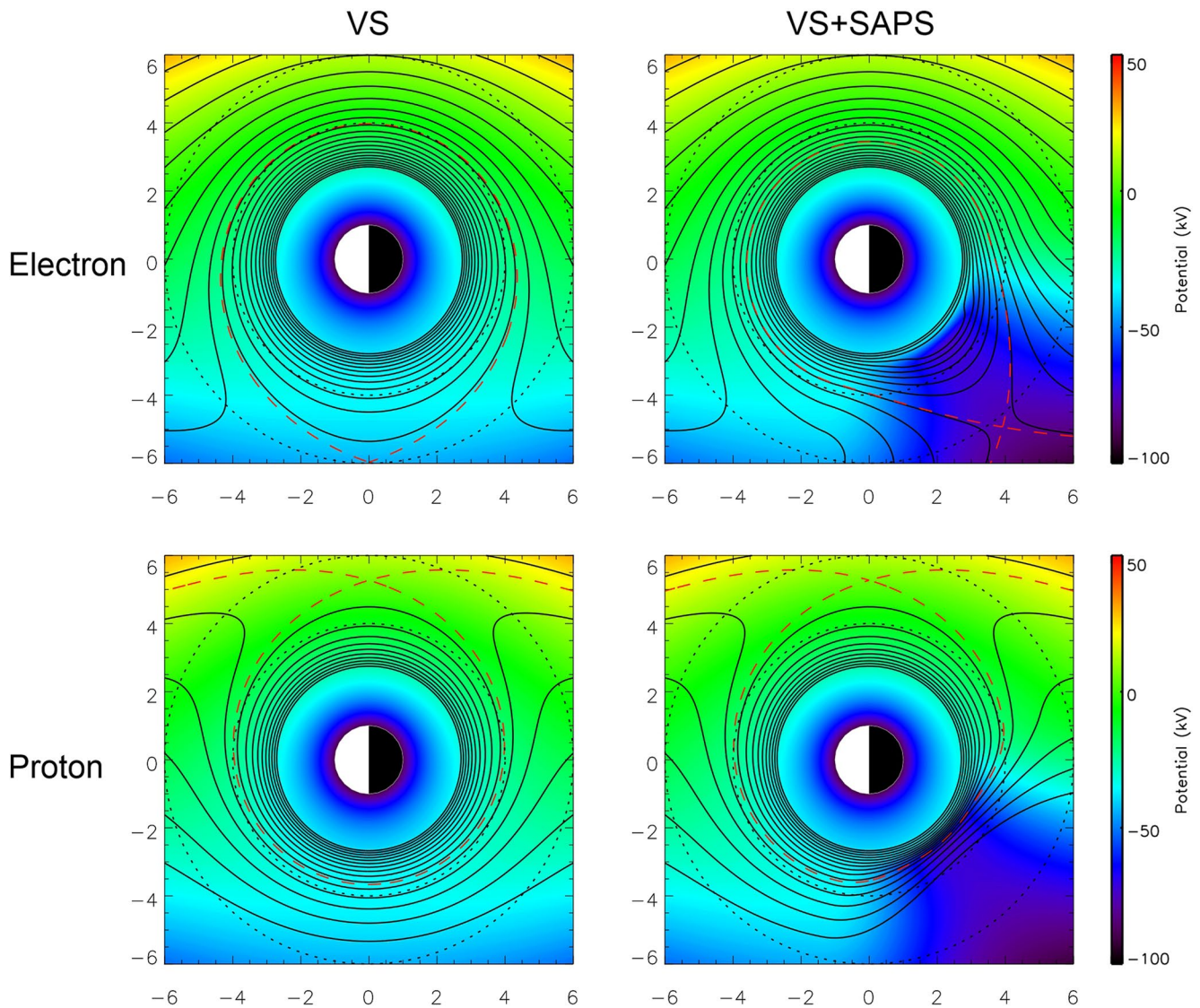
Figure 10. Drift paths for 10 MeV/G electrons (top panels) and protons (bottom panels) under the influence of Volland-Stern (left panels) and combined Volland-Stern and subauroral polarization streams (SAPS) electric fields (right panels). The dashed red lines indicate the open/closed drift path separatrix, and the color represents the electric potential. The two dotted circles indicate $L = 4$ and $L = 6$, respectively.

remain at lower L shells over a large range of MLT before drifting radially outward. This allows deeper penetration of plasma sheet electrons into the inner magnetosphere and increases the probability that the electrons will become trapped as the convection pattern changes. The addition of SAPS also allows the protons on open drift paths to reach lower L shells than for the Volland-Stern model, but only in a very limited MLT sector in the SAPS region; thus, these protons are not likely to become trapped.

The SAPS electric field also has effects on energetic particles that were previously trapped within the inner magnetosphere. Figure 11 shows the drift trajectories of an electron (left) and a proton (right) under the influence of the Volland-Stern electric field only (dashed lines) and the combined Volland-Stern and SAPS electric field (solid lines). The electron that originated inside the SAPS region (black dot in the left panel, $L = 4$, MLT = 21) is transported further inward under the SAPS electric field compared to the situation with Volland-Stern electric field alone, with an inward displacement $L \sim 0.5$ at dawn. On the contrary, the proton originating inside the SAPS region (black dot in the right panel, $L = 3.1$, MLT = 21) drifts further outward under the influence of SAPS electric field compared to the Volland-Stern electric field. These results suggest that the SAPS electric field has differential effects on trapped energetic electrons and protons: It transports trapped electrons inward and trapped
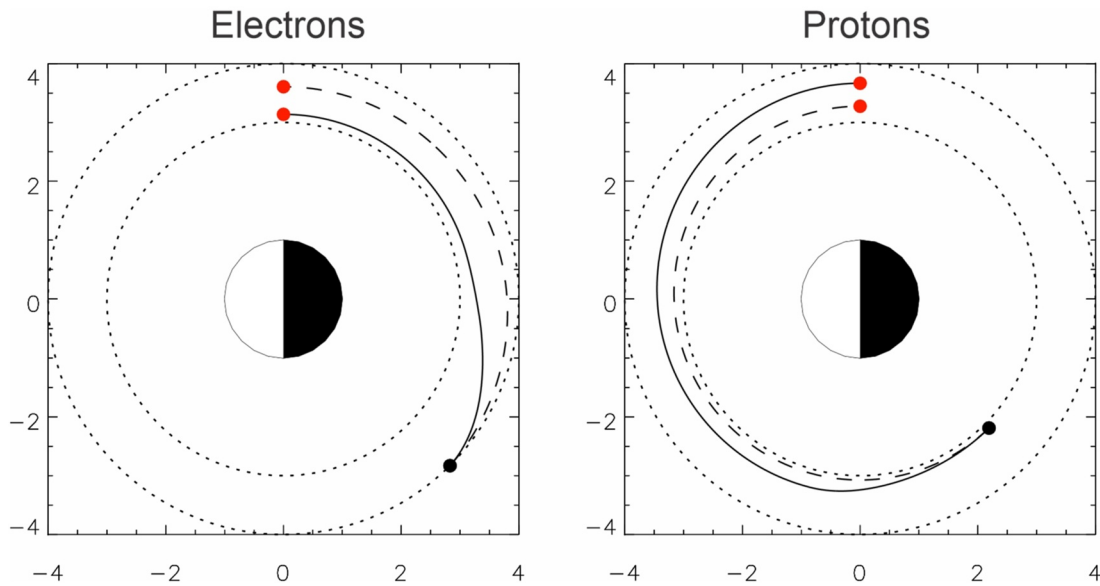
Figure 11. Electron (left) and proton (right) drift trajectories under the Volland-Stern electric field alone (dashed lines) and under the combined Volland-Stern and SAPS electric fields (solid lines). The electron starts from $L = 4$, MLT = 21 (black dot) and drifts eastward toward dawn (red dot); the proton starts from $L = 3.1$, MLT = 21 (black dot) and drifts westward toward dawn (red dot).

protons outward. This further contributes to the deeper penetration of energetic electrons than protons in the inner magnetosphere.

The simple electric field model demonstrates that, under the effect of the SAPS electric field, energetic electrons can penetrate to lower L compared to the situation with the Volland-Stern electric field alone. The progressive flux enhancements for electrons moving to lower L shells observed in all three events suggest that the electrons are transported inward in stages over several hours. This can be explained by the highly variable nature of convection and SAPS electric fields. Variations in convection and SAPS temporarily open drift paths to lower L shells, where the electrons become trapped as they drift around the day side and the convection pattern changes. These electrons are then transported further inward by additional convection and SAPS surges. We recognize that this simple model does not capture true spatial and temporal variability of SAPS. However, the model does demonstrate that a radial potential drop over a limited range of MLT allows electrons to penetrate to lower L shells than protons. Future work involves particle tracing using coupled magnetosphere-ionosphere simulations to investigate the impact of the temporal and spatial variation of SAPS on the energetic particle dynamics.

The drift path analysis is also consistent with the observations of protons in this study. During intervals when 100s keV electrons penetrated to low L shells, no enhancements of 100s keV protons were observed at these low L shells, suggesting a differential effect of SAPS electric field on electrons and protons. While lower-energy (50–100 keV) proton enhancements were observed at low L shells, they only occurred in the SAPS region on the dusk side and did not persist at low L shells on subsequent passes. This was most apparent in the 15 July 2015 and 7 September 2015 events when the spacecraft sampled the post-dusk and noon sectors, and the 10 MeV/G proton phase space density gradient was consistently located more earthward at dusk than at noon. We interpret this as a consequence of the outward radial drift for protons in the western portion of the SAPS region, which occurs at the same time that the electrons are transported radially inward in the eastern portion of the SAPS.

An azimuthal electric field is required to transport particles radially and energize/de-energize charged particles. Duskside SAPS electric field measurements in these events were strongest in the radial component, and tended to have a smaller eastward azimuthal component that transports particles radially outward. This eastward azimuthal electric field on the dusk side arises from the radial potential drop over a limited range of MLT, and a corresponding western azimuthal electric field and inward radial transport are expected on the eastern edge of the SAPS, likely in the midnight-predawn sector.

One interesting aspect of the differential response between the electrons and protons is that the lower energy particles (∼1–10 keV) which form the SAPS have the opposite behavior; at lower energies, the protons reach lower L shells than electrons, forming the pressure gradient and field-aligned currents that close at lower latitudes than the precipitating electron boundary. Our interpretation is that SAPS is a dynamic response to enhanced convection driven by the solar wind, where the initial convection onset brings the protons closer to Earth than the electrons in the post-dusk sector, setting up the SAPS. The SAPS electric field then affects the previously trapped higher-energy populations, and allows the higher-energy electrons to reach lower L shells than the protons.

7. Conclusions

This study explored the relationship between SAPS electric fields and 100s keV particle dynamics at low L shells in the inner magnetosphere. Van Allen Probes data were examined for three events covering moderate to intense geomagnetic activity levels, revealing a consistent picture of deep, sustained penetration of 100s keV electron fluxes during intervals when SAPS were observed at similar L shells, and little variation in the 100s keV proton fluxes in the same region. The electron phase space density gradients moved progressively radially inward, in some cases by 0.5 L in 1.5 hr, and lower-energy electrons reached lower L shells. The inward motion of the steep radial phase space density gradient for electrons suggests that inward radial transport is the dominant acceleration mechanism. 50–100 keV proton flux enhancements were observed in the SAPS region, but the enhancements did not persist on subsequent orbits at different local times, indicating that the protons were not trapped.

The differential response between the electrons and protons can be explained by the strong SAPS electric fields, which modify the drift paths of energetic particles and allow electrons to reach lower L shells than protons with similar energies. Analysis of the drift paths using a simple SAPS model and the Volland-Stern convection electric field demonstrated that the electrons can be transported radially inward on the easter edge of the SAPS and remain at low L shells on the dayside, which allows the electrons to be trapped deep within the inner magnetosphere. The protons, on the other hand, are also transported radially inward on the eastern edge of the SAPS, but are quickly transported back outward as they drift westward through the SAPS region. Observations of progressive inward motion and sustained electron fluxes at low L shells, and only temporary lower-energy proton flux enhancements in the SAPS region are consistent with this picture.

This study demonstrates that SAPS are present in the correct place and time to affect the 100s keV particle dynamics in the inner magnetosphere, and the particle observations are qualitatively consistent with predictions using a SAPS electric field model. The SAPS electric fields presented here were persistent over 1.5–4 hr between successive Van Allen Probes passes, and the amplitude and spatial structure was variable. The dynamic picture would benefit from a lager constellation of multipoint measurements, as the timescales of the electric field variations and inward radial transport of electrons are shorter than the resample period of the Van Allen Probes. Future work includes particle tracing using coupled magnetosphere-ionosphere models to augment the Van Allen Probes observations.

Data Availability Statement

All RBSP-ECT data are publicly available at the website https://rbsp-ect.newmexicoconsortium.org/science/DataDirectories.php. The RBSPICE instrument was supported by JHU/APL Subcontract No. 937836 to the New Jersey Institute of Technology under NASA Prime Contract No. NAS5-01072. RBSPICE data are available at http://rbspice.ftecs.com. The work by the EFW team was conducted under JHU/APL contract 922,613 (RBSP-EFW). EFW data are available at http://www.space.umn.edu/rbspefw-data/. EMFISIS data are available at https://emfisis.physics.uiowa.edu/data/index. The solar wind and geomagnetic data are available at OmniWeb http://omniweb.gsfc.nasa.gov.

References

Anderson, P. C., Carpenter, D. L., Tsuruda, K., Mukai, T., & Rich, F. J. (2001). Multisatellite observations of rapid subauroral ion drifts (SAID). *Journal of Geophysical Research*, *106*(A12), 29585–29599 https://doi.org/10.1029/2001JA000128

Berko, F. W., Cahill, L. J., Jr, & Fritz, T. A. (1975). Protons as the prime contributors to storm time ring current. *Journal of Geophysical Research*, *80*(25), 3549–3552. https://doi.org/10.1029/JA080i025p03549

Blake, J. B., Carranza, P. A., Claudepierre, S. G., Clemmons, J. H., Crain, Jr, W. R., Dotan, W. R., et al. (2013). The magnetic electron ion spectrometer (MagEIS) instruments aboard the radiation belt storm probes (RBSP) spacecraft. *Space Science Reviews*, *179*, 383–421. https://doi.org/10.1007/s11214-013-9991-8

Bortnik, J., & Thorne, R. M. (2007). The dual role of ELF/VLF chorus waves in the acceleration and precipitation of radiation belt electrons. *Journal of Atmospheric and Solar-Terrestrial Physics*, *69*(3), 378–386. https://doi.org/10.1016/j.jastp.2006.05.030

Califf, S., Li, X., Blum, L., Jaynes, A., Schiller, Q., Zhao, H., & Bonnell, J. W. (2014). THEMIS measurements of quasi-static electric fields in the inner magnetosphere. *Journal of Geophysical Research: Space Physics*, *119*(12), 9939–9951. https://doi.org/10.1002/2014JA020360

Califf, S., Li, X., Zhao, H., Kellerman, A., Sarris, T. E., Jaynes, A., & Malaspina, D. M. (2017). The role of the convection electric field in filling the slot region between the inner and outer radiation belts. *Journal of Geophysical Research: Space Physics*, *122*(2), 2051–2068. https://doi.org/10.1002/2016JA023657

Daglis, I. A., Thorne, R. M., Baumjohann, W., & Orsini, S. (1999). The terrestrial ring current: Origin, formation, and decay. *Reviews of Geophysics*, *37*(4), 407–438. https://doi.org/10.1029/1999RG900009

Foster, J. C., & Burke, W. J. (2002). SAPS: A new categorization for sub-auroral electric fields. *Eos, Transactions of the American Geophysical Union*, *83*(36), 393–394. https://doi.org/10.1029/2002EO000289

Foster, J. C., Erickson, P. J., Coster, A. J., Thaller, S., Tao, J., Wygant, J. R., et al. (2014). Storm time observations of plasmasphere erosion flux in the magnetosphere and ionosphere. *Geophysical Research Letters*, *41*, 762–768. https://doi.org/10.1002/2013GL059124

Foster, J. C., & Vo, H. B. (2002). Average characteristics and activity dependence of the subauroral polarization stream. *Journal of Geophysical Research*, *107*(A12), 1475. https://doi.org/10.1029/2002JA009409

Funsten, H. O., Skoug, R. M., Guthrie, A. A., MacDonald, E. A., Baldonado, J. R., Harper, R. W., et al. (2013). Helium, Oxygen, Proton, and Electron (HOPE) mass spectrometer for the radiation belt storm probes mission. *Space Science Reviews*, *179*(1–4), 423–484. https://doi.org/10.1007/s11214-013-9968-7

Galperin, Y., Ponomarev, V. N., & Zosimova, A. G. (1974). Plasma convection in the polar ionosphere. *Annals of Geophysics*, *30*(1).

Galperin, Y. I., Ponomarov, Y. N., & Zosinova, A. G. (1973). Direct measurements of ion drift velocity in the upper ionosphere during a magnetic storm. *Cosmicheskie Issled*, *11*, 273.

Gkioulidou, M., Ukhorskiy, A. Y., Mitchell, D. G., & Lanzerotti, L. J. (2016). Storm time dynamics of ring current protons: Implications for the long-term energy budget in the inner magnetosphere. *Geophysical Research Letters*, *43*(10), 4736–4744. https://doi.org/10.1002/2016GL068013

Goldstein, J., Burch, J. L., & Sandel, B. R. (2005). Magnetospheric model of subauroral polarization stream. *Journal of Geophysical Research: Space Physics*, *110*(A9). https://doi.org/10.1029/2005JA011135

Horne, R. B., Thorne, R. M., Glauert, S. A., Meredith, N. P., Pokhotelov, D., & Santolík, O. (2007). Electron acceleration in the Van Allen radiation belts by fast magnetosonic waves. *Geophysical Research Letters*, *34*(17). https://doi.org/10.1029/2007GL030267

Kanekal, S. G., Baker, D. N., Fennell, J. F., Jones, A., Schiller, Q., Richardson, I. G., et al. (2016). Prompt acceleration of magnetospheric electrons to ultrarelativistic energies by the 17 March 2015 interplanetary shock. *Journal of Geophysical Research: Space Physics*, *121*(8), 7622–7635. https://doi.org/10.1002/2016JA022596

Kletzing, C. A., Kurth, W. S., Acuna, M., MacDowall, R. J., Torbert, R. B., Averkamp, T., et al. (2013). The electric and magnetic field instrument suite and integrated science (EMFISIS) on RBSP. *Space Science Reviews*, *179*(1–4), 127–181. https://doi.org/10.1007/s11214-013-9993-6

Korth, H., Thomsen, M. F., Borovsky, J. E., & McComas, D. J. (1999). Plasma sheet access to geosynchronous orbit. *Journal of Geophysical Research: Space Physics*, *104*(A11), 25047–25061. https://doi.org/10.1029/1999JA900292

Kunduri, B. S. R., Baker, J. B. H., Ruohoniemi, J. M., Thomas, E. G., Shepherd, S. G., & Sterne, K. T. (2017). Statistical characterization of the large-scale structure of the subauroral polarization stream. *Journal of Geophysical Research: Space Physics*, *122*, 6035–6048. https://doi.org/10.1002/2017JA024131

Kurth, W. S., De Pascuale, S., Faden, J. B., Kletzing, C. A., Hospodarsky, G. B., Thaller, S., et al. (2015). Electron densities inferred from plasma wave spectra obtained by the Waves instrument on Van Allen Probes. *Journal of Geophysical Research: Space Physics*, *120*, 904–914. https://doi.org/10.1002/2014JA020857

Lejosne, S., Kunduri, B. S., Mozer, F. S., & Turner, D. L. (2018). Energetic electron injections deep into the inner magnetosphere: A result of the subauroral polarization stream (SAPS) potential drop. *Geophysical Research Letters*, *45*(9), 3811–3819. https://doi.org/10.1029/2018GL077969

Li, X., Roth, I., Temerin, M., Wygant, J. R., Hudson, M. K., & Blake, J. (1993). Simulation of the prompt energization and transport of radiation belt particles during the March 24, 1991 SSC. *Geophysical Research Letters*, *20*(22), 2423–2426. https://doi.org/10.1029/93GL02701

Lyons, L. R., Gallardo-Lacourt, B., Zou, S., Weygand, J. M., Nishimura, Y., Li, W., et al. (2016). The 17 March 2013 storm: Synergy of observations related to electric field modes and their ionospheric and magnetospheric effects. *Journal of Geophysical Research: Space Physics*, *121*(11) 10880–10897. https://doi.org/10.1002/2016JA023237

Matsui, H., Jordanova, V. K., Quinn, J. M., Torbert, R. B., & Paschmann, G. (2004). Derivation of electric potential patterns in the inner magnetosphere from Cluster EDI data: Initial results. *Journal of Geophysical Research*, *109*, A10202. https://doi.org/10.1029/2003JA010319

Matsui, H., Puhl-Quinn, P. A., Jordanova, V. K., Khotyaintsev, Y., Lindqvist, P.-A., & Torbert, R. B. (2008). Derivation of inner magnetospheric electric field (UNH-IMEF) model using Cluster data set. *Annals of Geophysics*, *26*, 2887–2898. https://doi.org/10.5194/angeo-26-2887-2008

Matsui, H., Torbert, R. B., Spence, H. E., Khotyaintsev, Y. V., & Lindqvist, P.-A. (2013). Revision of empirical electric field modeling in the inner magnetosphere using Cluster data. *Journal of Geophysical Research: Space Physics*, *118*(7), 4119–4134. https://doi.org/10.1002/jgra.50373

Maynard, N. C., & Chen, A. J. (1975). Isolated cold plasma regions: Observations and their relation to possible production mechanisms. *Journal of Geophysical Research*, *80*, 1009–1013. https://doi.org/10.1029/JA080i007p01009

Mitchell, D. G., Lanzerotti, L. J., Kim, C. K., Stokes, M., Ho, G., Cooper, S., et al. (2013). Radiation belt storm probes ion composition experiment (RBSPICE). *Space Science Reviews*, *179*, 263–308. https://doi.org/10.1007/s11214-013-9965-x

Reeves, G. D., Friedel, R. H., Larsen, B. A., Skoug, R. M., Funsten, H. O., Claudepierre, S. G., et al. (2016). Energy-dependent dynamics of keV to MeV electrons in the inner zone, outer zone, and slot regions. *Journal of Geophysical Research: Space Physics*, *121*(1), 397–412. https://doi.org/10.1002/2015JA021569

Rowland, D. E., & Wygant, J. R. (1998). Dependence of the large-scale, inner magnetospheric electric field on geomagnetic activity. *Journal of Geophysical Research: Space Physics*, *103*(A7), 14959–14964. https://doi.org/10.1029/97JA03524

Schiller, Q., Kanekal, S. G., Jian, L. K., Li, X., Jones, A., Baker, D. N., et al. (2016). Prompt injections of highly relativistic electrons induced by interplanetary shocks: A statistical study of van allen probes observations. *Geophysical Research Letters*, *43*(24), 12–317. https://doi.org/10.1002/2016GL071628

Smiddy, M., Kelley, M. C., Burke, W., Rich, F., Sagalyn, R., Shuman, B., et al. (1977). Intense poleward-directed electric fields near the ionospheric projection of the plasmapause. *Geophysical Research Letters*, *4*(11), 543–546. https://doi.org/10.1029/GL004i011p00543

Smith, P. H., & Hoffman, R. A. (1973). Ring current particle distributions during the magnetic storms of December 16–18, 1971. *Journal of Geophysical Research*, *78*(22), 4731–4737. https://doi.org/10.1029/JA078i022p04731

Spiro, R. W., Heelis, R. A., & Hanson, W. B. (1979). Rapid subauroral ion drifts observed by Atmosphere Explorer C. *Geophysical Research Letters*, *6*(8), 657–660. https://doi.org/10.1029/GL006i008p00657

Stern, D. P. (1975). The motion of a proton in the equatorial magnetosphere. *Journal of Geophysical Research*, *80*, 595–599. https://doi.org/10.1029/JA080i004p00595

Su, Y. J., Selesnick, R. S., & Blake, J. B. (2016). Formation of the inner electron radiation belt by enhanced large-scale electric fields. *Journal of Geophysical Research: Space Physics*, *121*(9), 8508–8522. https://doi.org/10.1002/2016JA022881

Tsyganenko, N. A. (1989). A magnetospheric magnetic field model with a warped tail current sheet. *Planetary and Space Science*, *37*(1), 5–20. https://doi.org/10.1016/0032-0633(89)90066-4

Turner, D. L., Claudepierre, S. G., Fennell, J. F., O'Brien, T. P., Blake, J. B., Lemon, C., et al. (2015). Energetic electron injections deep into the inner magnetosphere associated with substorm activity. *Geophysical Research Letters*, *42*(7), 2079–2087. https://doi.org/10.1002/2015GL063225

Turner, D. L., O'Brien, T. P., Fennell, J. F., Claudepierre, S. G., Blake, J. B., Jaynes, A. N., et al. (2017). Investigating the source of near-relativistic and relativistic electrons in Earth's inner radiation belt. *Journal of Geophysical Research: Space Physics*, *122*, 695–710. https://doi.org/10.1002/2016JA023600

Volland, H. (1973). A semiempirical model of large-scale magnetospheric electric fields. *Journal of Geophysical Research*, *78*, 171–180. https://doi.org/10.1029/JA078i001p00171

Williams, D. J. (1980). Ring current composition and sources. In S.-I. Akasofu (Ed.), *Dynamics of the magnetosphere* (p. 407424). Dordrecht: D. Reidel Co.. https://doi.org/10.1007/978-94-009-9519-2_21

Wygant, J., Bonnell, J. W., Goetz, K., Ergun, R. E., Mozer, F. S., Bale, S. D., et al. (2013). *The electric field and waves instruments on the radiation belt storm probes mission*. The Van Allen Probes Mission, 183–220. https://doi.org/10.1007/978-1-4899-7433-4_6

Yu, Y., Jordanova, V., Zou, S., Heelis, R., Ruohoniemi, M., & Wygant, J. (2015). Modeling subauroral polarization streams during the 17 March 2013 storm. *Journal of Geophysical Research: Space Physics*, *120*, 1738–1750. https://doi.org/10.1002/2014JA020371

Zhao, H., Baker, D. N., Califf, S., Li, X., Jaynes, A. N., Leonard, T., et al. (2017). Van Allen probes measurements of energetic particle deep penetration into the low L region (L < 4) during the storm on 8 April 2016. *Journal of Geophysical Research: Space Physics*, *122*(12), 140–12,152. https://doi.org/10.1002/2017JA024558

Zhao, H., & Li, X. (2013). Inward shift of outer radiation belt electrons as a function of Dst index and the influence of the solar wind on electron injections into the slot region. *Journal of Geophysical Research: Space Physics*, *118*(2), 756–764. https://doi.org/10.1029/2012JA018179

Zhao, H., Li, X., Baker, D. N., Claudepierre, S. G., Fennell, J. F., Blake, B. J., et al. (2016). Ring current electron dynamics during geomagnetic storms based on the Van Allen Probes measurements. *Journal of Geophysical Research: Space Physics*, *121*, 3333–3346. https://doi.org/10.1002/2016JA022358

Zhao, H., Li, X., Baker, D. N., Fennell, J. F., Blake, J. B., Larsen, B. A., et al. (2015). The evolution of ring current ion energy density and energy content during geomagnetic storms based on Van Allen Probes measurements. *Journal of Geophysical Research: Space Physics*, *120*, 7493–7511. https://doi.org/10.1002/2015JA021533